Supplemental information for "Terraced deposits linked to periodic collapse of caldera-forming eruption columns"

October 6, 2022

Johan T. Gilchrist[1*] (jgilchri@eoas.ubc.ca), A. Mark Jellinek[1] (mjellinek@eoas.ubc.ca),
Sean Wanket[1] (swanket@eoas.ubc.ca), Emilie E. E. Hooft[2] (emilie@uoregon.edu)
[1] Earth, Ocean and Atmospheric Sciences, UBC [2] Earth Sciences, UO

Here we show additional results from ours and previous studies to support our discussion of links between volcanic jet dynamics and terracing of catastrophic caldera eruption deposits. First, we describe the supplemental videos of select analog experiments. Second, we analyze the published radial bathymetry and seismic reflection profiles of Macauley caldera's deposit terracing and interpret it on the basis of our experimental results. Third, we show results from spectral analysis of radial deposit profiles from a shallow water experiment to compare with deep water experiment deposits. Fourth, we show how jet height oscillations are linked to sedimentation wave dynamics in both deep water and shallow water scenarios. Fifth, we show how the penetration depth of sedimentation waves into a shallow water layer governs the extent to which the near-vent deposit is scoured. Sixth, we highlight deposit terraces surrounding the caldera of Somma-Vesuvius. Finally, we show that deposit terracing occurs for jets in the Total Collapse regime with cylindrical and annular nozzle profiles.

1 Supplemental Videos of experiments

1. **Supplemental Video 1**: Front and top views of shallow water experiment 1 synchronized in time. Shows sedimentation waves descending from oscillating fountain top, sedimentation wave spreading at the air-water interface and the generation of waves analogous to tsunamis.

2. **Supplemental Video 2**: Front and top views of shallow water experiment 11 synchronized in time. Shows similar dynamics as Supplemental Video 1 as well as development of the "groovy instability" in ground-hugging gravity currents that deposits spoke-like particle ridges in the deposit and scalloping of terraces [cf. Figure 4 in main text].

3. **Supplemental Video 3**: Front and top views of deep water experiment 15 synchronized in time. The groovy instability is expressed as lobes and clefts in the spreading ground-hugging gravity current fronts.

4. **Supplemental Video 4**: Oblique and front views of deep water experiment 10 synchronized in time. As the fountain mixture reaches the water surface, mass is partitioned into descending sedimentation waves and surges of clouds just below the water surface that form a spoke-like pattern (pink clouds in top view frame). The spoke-like pattern of surging clouds is interpreted to be an expression of the groovy instability occurring in water surface-hugging gravity currents.

2 Macauley caldera terracing

In addition to the shallow submarine CCF eruption deposits of Sumisu and Santorini, Macauley Caldera on the Kermadec Arc also shows striking terraces that parallel the caldera rim (Figure 2; Pope et al., 2018). Broad, backward-facing concave terraces in the near-field decrease continuously in wavelength with radial distance from the caldera rim, in agreement with the morphology of our shallow water experiment deposits [Figures 1c-d & 2f]. Between the caldera rim and first terrace there is a upwardly-curved depression that is 2-4 times the wavelength of the adjacent near-field terraces [Figure 2b]. On the basis of our shallow water experiments, we interpret this feature as a sedimentation wave impact zone where the distance from the caldera rim to the first terrace is r_{im} (Figure 1e,f) and the upward curvature is the expression of deposit scouring driven as a result of sedimentation waves impacting the seabed as jets in a $D_{sw} \leq 1$ limit [cf. Figure 3 and 4c in main text].

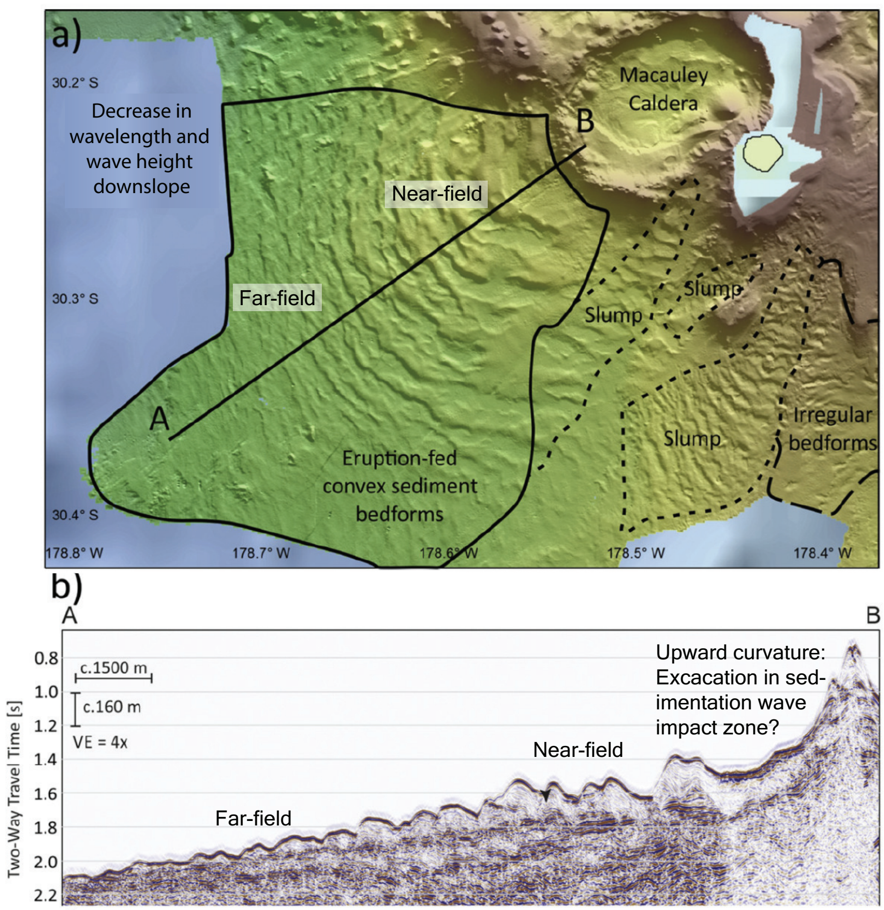

Figure 1: | **Macauley caldera deposit bathymetry and subsurface.** Bathymetry of the terraced pyroclastic deposit surrounding Macauley caldera (Kermadec arc, 5.7 ka or unknown, Barker et al., 2012), showing terrace λ_T decreasing with increasing radial distance from the caldera (From Pope et al., 2018, . Used with permission from Elsevier). **d)** Seismic profile A-B shown in f) showing decreasing λ_T terrace crest height with radial distance from caldera Pope et al. (2018).

3 Additional shallow water experiment terracing profiles

In addition to deep water experiments, shallow water deposits also show axisymmetric terracing [Figure S2]. Similarly to deep water experiments, spectral analysis of radial deposit topography profiles show that terraces have relatively long wavelengths in the near-field that decrease in wavelength moving radially outward to the far-field [Figure S2a]. Wavelengths identified in the radial deposit topography profile spectra are confirmed by direct measurement of terrace wavelengths in deposit images [Figure S2b].

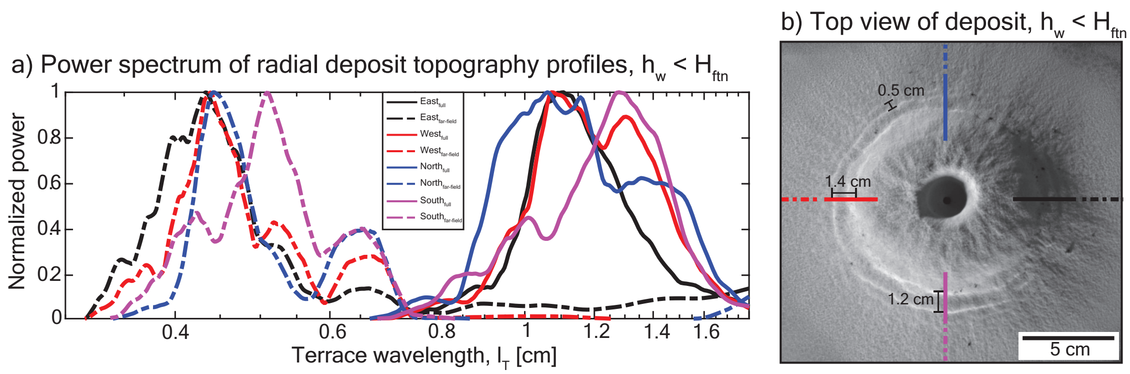

Figure 2: | **Power spectrum of shallow water terraced deposit. a)** Power spectra of radial deposit topographic profiles color coordinated to their locations in b) for experiment #11. Solid lines are power spectra taken across relatively large λ_T terraces and dotted lines are separate power spectra taken across relatively small λ_T where the profiles are high pass filtered to exclude the relativley large λ_T signal. **b)** Peaks in power spectra in a) correspond to $0.45\lambda_T \leq 0.5$ cm and $1.1 \leq \lambda_T \leq 1.4$ cm.

4 Geometry, dynamics and utility of volcanic "fountain" height oscillations in greater detail

Analog eruption columns in the TC regime are examples of multiphase turbulent fountains that rise to time-averaged heights H_{ftn} governed by a balance between the driving momentum flux carried by the injected mixture and the restoring buoyancy effects supplied by the density stratification. Sedimentation waves descend approximately from H_{ftn} to an impact zone on the ground/seabed with radius r_{im}, which is about 3 times the vent radius in subaerial or deep-water limits (Figure 5a-b; Gilchrist and Jellinek, 2021) and larger for shallow water conditions, as is discussed in detail in the text. The excitation, growth and descent of sedimentation waves induces oscillations around a mean height H_{ftn} with a characteristic frequency f_{ftn} discussed in the text that is distinct from the buoyancy frequency N, which indicates the response of the stabilizing environmental density stratificatio (Burridge and Hunt, 2013; Gilchrist and Jellinek, 2021). Where $f_{ftn} > N$, the frequencies of

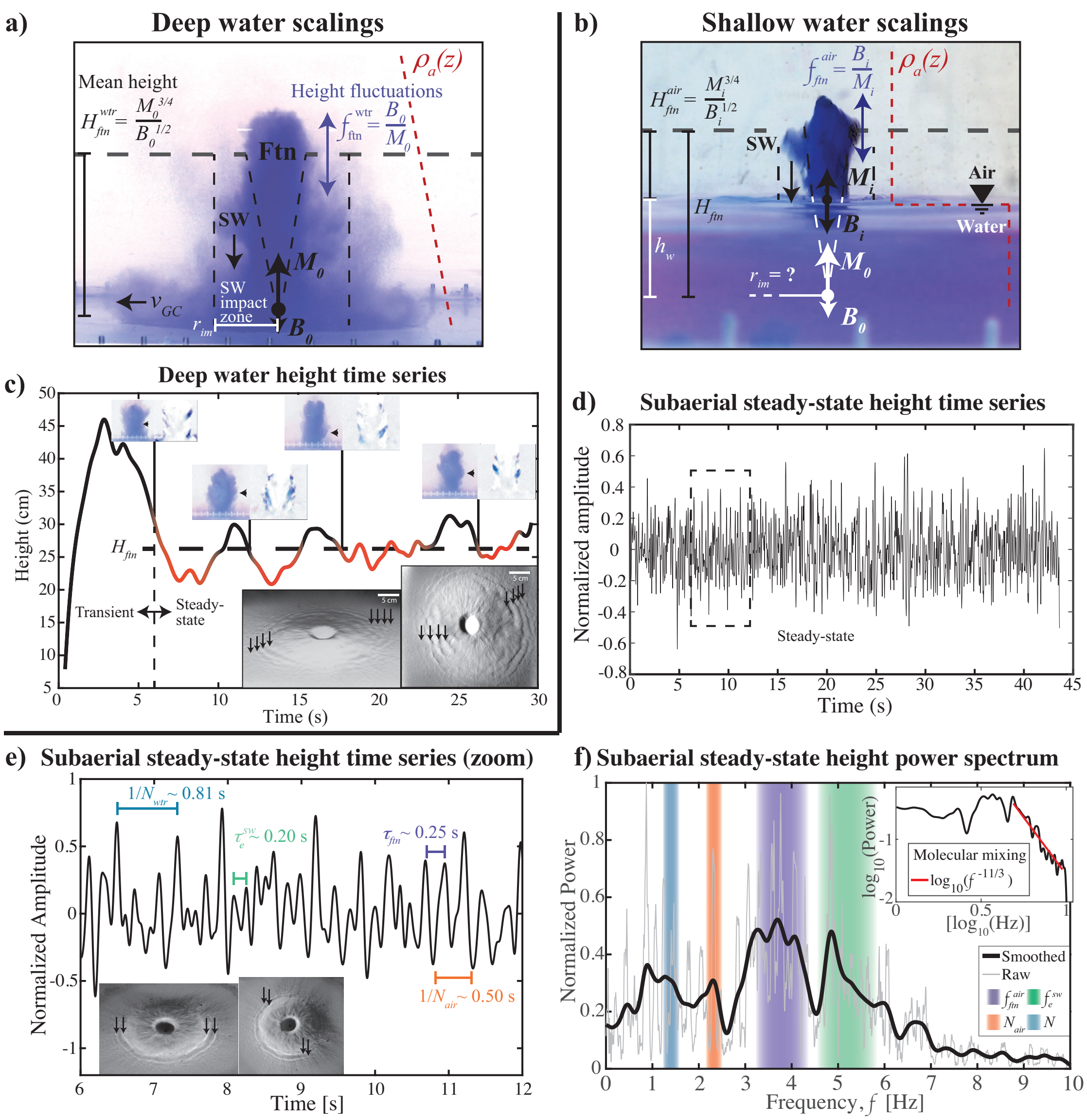

Figure 3: | **Fountain source parameters, top height oscillations, and sedimentation wave frequency .**

Figure 3: | **Fountain source parameters, top height oscillations, and sedimentation wave frequency .** **a)** Image of a coarse particle fountain midway through a deep water experiment where sand-saltwater mixtures appear purple and ambient saltwater is transparent. The upflowing region of the fountain is marked "Jet", descending sedimentation wave "SW", radius of the sedimentation wave impact zone r_{im}, the ground-hugging gravity current spread speed v_{GC}, and the density stratification of the ambient saltwater layer $\rho_a(z)$. **b)** Image of a coarse particle fountain breaching the air-water interface midway through a shallow water experiment. **c)** Fountain top height time series for deep water experiment #32. Inset fountain images highlight sedimentation waves with black arrows on left side and wave fronts in purple on right side. Black arrows indicate terraces in deposit inset images. **d)** Fountain top height time series for shallow water experiment #11. **e)** Zoomed section of shallow water fountain top height time series (dotted box in d) where the sedimentation wave overturn, fountain collapse and stratification oscillation periods are identified. Inset deposit images show two distinct terraces. **f)** Power spectrum of fountain top height fluctuations. Inset graph shows power spectrum in log-log space with red curve (Ozimidov scaling law) indicating energy dissipation through irreversible mixing across density interfaces Ozmidov (1965); Gilchrist and Jellinek (2021).

sediment waves descending along fountain margins will be determined by both f_{ftn} and N, whereas where $f_{ftn} < N$ the frequencies of these processes will be determined solely by the stratification, N (see (Gilchrist and Jellinek, 2021)).

For deep water fountains, depending on jet source conditions (see Figure 3 in the text), the relatively low frequencies and high amplitudes of fountain top height oscillations are governed by f_{ftn} and the frequency at which the ambient density stratification oscillates in response to the perturbation of the fountain,

$$N = \sqrt{-\frac{g}{\rho_{a,0}}\frac{\mathrm{d}\rho_a(z)}{\mathrm{d}z}}, \tag{1}$$

where $\rho_{a,0}$ is the ambient density at the source height and the density stratification $\mathrm{d}\rho_a(z)/\mathrm{d}z$ is assumed to be linear [Figure S3a].

For shallow water fountains breaching the water surface there are three additional frequencies that can contribute fountain height oscillation modes: 1) f_{ftn}^{air} defined for the subaerial part of the fountain; 2) the restoring stratification frequency N of the combined water and air layers, defined with the density difference between the water layer and air over the maximum fountain rise height through both layers; and 3) N_{air} of the air layer defined using the density difference between the water layer and air over the subaerial fountain rise height [Figure S3b]. Low frequency and high amplitude fountain height oscillations are governed by N and N_{air} whereas f_{ftn}^{air} governs relatively higher frequency and lower amplitude oscillations. Fountain top oscillations are an expression of the build up and collapse of periodic sedimentation waves around the upflowing fountain core [Figure S3a-b]. An additional mode evident in time series of column heights is related to inertial effects of the overturning motions characterizing stirring as well as entrainment and mixing across density interfaces as SWs descend:

$$f_e^{sw} = \frac{u_{sw}}{r_{sw}}. \tag{2}$$

Usefully and significantly, we predict SWs to excite a distinctive and easily-recognized fountain top oscillation corresponding to this frequency (see Gilchrist and Jellinek (2021)).

Fountain height oscillation results In deep water experiments, the fountain rises to an initial global maximum height defining the transient period of an experiment and then lowers to mean height defining the steady-state phase of the remainder of the experiment, the latter of which is the focus of our height oscillation analysis [Figure S3]. In experiment #32, prior to each height minima, a sedimentation wave is observed to descend around the fountain core [cf. red sections of curve with fountain image insets in Figure S3]. This process repeats at least four times during the steady-state phase and the resulting deposit has four distinct terraces that strongly suggests each sedimentation wave builds a single new terrace [deposit insets in Figure S3].

For shallow water experiment #11 four distinct oscillation periods are identified in the subaerial fountain top height time series [Figure S3e-f] and agree with predicted $1/f_{ftn}$, $1/N$ and $1/N_{air}$ from source and environmental conditions, as well as $1/f_e^{sw}$ measured by tracking sedimentation wave descent speed and radius. Overall, we find that shallow water fountains input energy to the stratification at f_{ftn}^{wtr} which is then dissipated to N, N_{air}, f_{ftn}^{air}, and f_e^{sw}, in that order. Above f_e^{sw} fountain height fluctuation energy dissipates according to a $\epsilon = f^{-11/3}$ power law associated with molecular mixing across the air-water density interface (Ozmidov, 1965).

5 Deposit scouring

The water depth and the momentum of jets as they penetrate the water layer, captured by D_{sw} [Equation 1 in main text], determines the radial extent of scouring in the near-field deposit [Figure S5]. Shallow water deposits with a scouring radius r_{sc} more than twice the radius of the vent indicate that the water depth was relatively shallow compared to the momentum of sedimentation waves. As the $D_{sw} \to 0$ the scoured area of the deposit increases substantially and a plateau of deposited particles may form around this area [top inset in Figure S5]. Deep water deposits with a scouring radius r_{sc} more than twice the radius of the vent indicate that sedimentation waves impacted the near-field deposit with enough momentum to scour the near-field deposit, however, r_{sc} is systematically shorter in deep water experiments compared to shallow water experiments. Indeed, the extent of near-field eruption deposit scouring can reveal whether descending sedimentation waves impacted with relatively high momentum to produce surging PDCs that entrain previously erupted material or with relatively low momentum to deposit particles in the impact zone.

Figure 4: | **Deposit scour radius as a function of sedimentation wave penetration depth.** Scoured radius r_{sc} of deposit as a function of sedimentation wave penetration depth D_{sw}. First two insets in each colored panel of images show a sedimentation wave descending around the subaerial region of a shallow water fountain and then impacting the air-water interface with r_{sw} marked. The third insets are top view images of the resulting deposit. Fourth insets in the middle (purple) and bottom (yellow) panels show the terraced deposits of Santorini and Sumsiu, respectively.

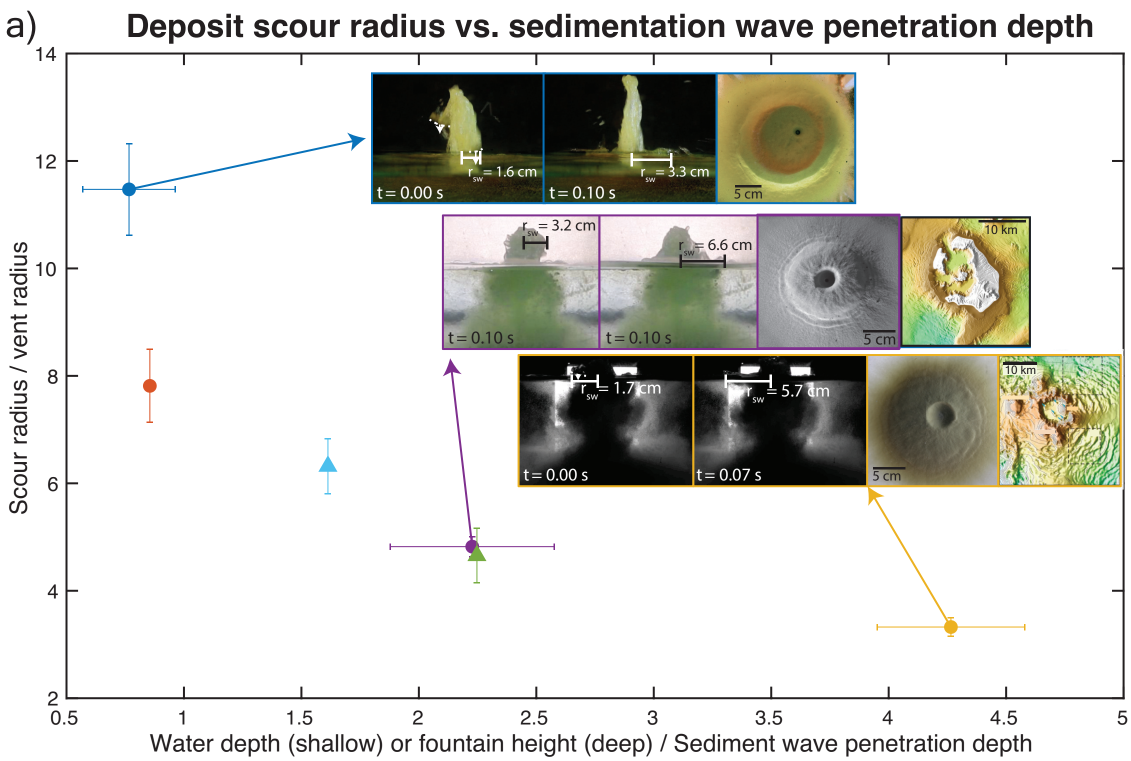

Figure 5: | **Deposit scour radius as a function of sedimentation wave penetration depth.**

6 Terracing around Somma-Vesuvius caldera

The deposit surrounding Somma-Vesuvius caldera may be the first robust example of a subaerial terraced CCF eruption deposit. Terraces appear to parallel the caldera rim of Somma-Vesuvius, suggesting that one or several of its eruptions since 22 ka (Cioni et al., 2008) may have occurred in the Total Collapse regime with MER$\geq 10^8$ kg/s [see Figure 3 in main text]. If true, this demonstrates that terraced deposits and periodic eruption column collapse are inherently linked to CCF eruptions in subaerial and submarine environments.

7 Terracing around cylindrical and annular nozzles

Deposit terracing occurs for deep water fountains injected through cylindrical or annular vent geometries [Figure S7]. Where relatively high total mass of particles are deposited, terraces forming early in an eruption may be buried by material erupted in later eruptive phases [Figure S7b & [Figure S7]d]. Whereas deep water experiments can form conical particle deposits around the vent and within the outermost visible terrace that can bury early-forming terraces, in shallow water experiments the analogous particle deposit forms relatively wide and concave plateau of particles [cf. Figures S2b & S7]. In both cases where terrace may potentially be buried in the near-field, ground-hugging flows (PDCs) accelerate as jets down cones or plateaus of injected (erupted) material that can excavate the deposit where the slope shallows and build new terraces just beyond the base of the cone or plateau.

Somma-Vesuvius topography

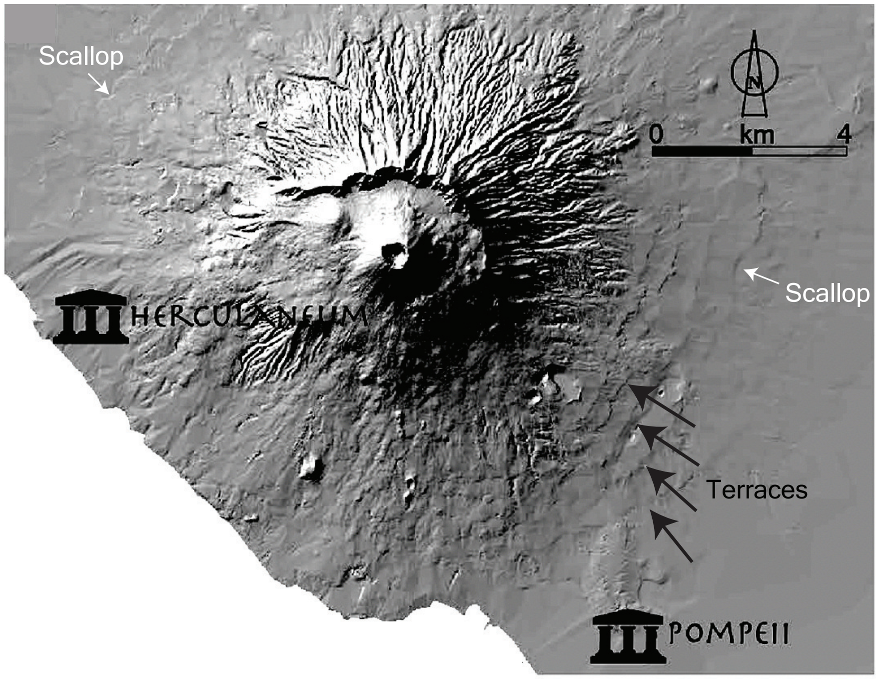

Figure 6: | **Terracing in the deposit surrounding Somma-Vesuvius caldera.** LIDAR-derived topographic model of the Somma-Vesuvius deposit Dellino et al. (2021). Apparent terracing and scalloping of the deposit are marked with black and white arrows respectively.

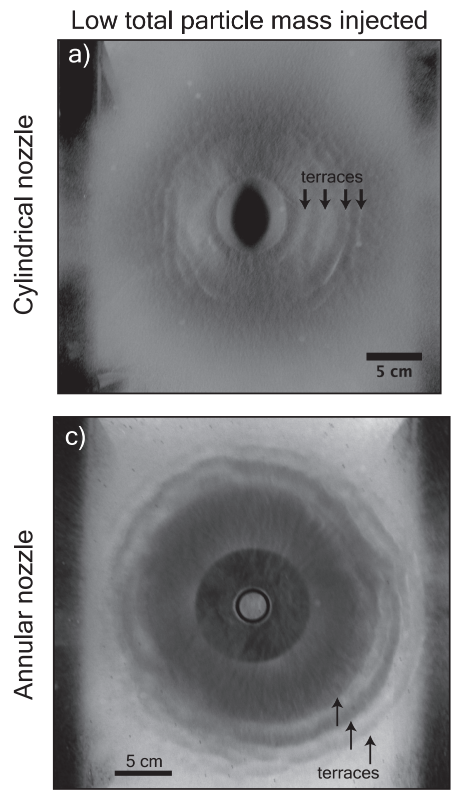

Figure 7: | **Deep water terraced deposits with low versus high total mass deposited.** Black arrows highlight terraces and particle cone at the angle of repose of the particles surrounding vent is marked.

References

Barker, S. J., Rotella, M. D., Wilson, C. J., Wright, I. C., and Wysoczanski, R. J. (2012). Contrasting pyroclast density spectra from subaerial and submarine silicic eruptions in the kermadec arc: implications for eruption processes and dredge sampling. *Bulletin of volcanology*, 74(6):1425–1443.

Burridge, H. and Hunt, G. (2013). The rhythm of fountains: the length and time scales of rise height fluctuations at low and high froude numbers. *Journal of Fluid Mechanics*, 728:91–119.

Cioni, R., Bertagnini, A., Santacroce, R., and Andronico, D. (2008). Explosive activity and eruption scenarios at somma-vesuvius (italy): towards a new classification scheme. *Journal of Volcanology and Geothermal Research*, 178(3):331–346.

Dellino, P., Dioguardi, F., Isaia, R., Sulpizio, R., and Mele, D. (2021). The impact of pyroclastic density currents duration on humans: the case of the ad 79 eruption of vesuvius. *Scientific Reports*, 11(1):1–9.

Gilchrist, J. T. and Jellinek, A. M. (2021). Sediment waves and the gravitational stability of volcanic jets. *Bulletin of Volcanology*, 83(10):1–59.

Ozmidov, R. V. (1965). On the turbulent exchange in a stably stratified ocean. *Atmospheric and Oceanic Physics Series1*, 1(8):853–860.

Pope, E. L., Jutzeler, M., Cartigny, M. J., Shreeve, J., Talling, P. J., Wright, I. C., and Wysoczanski, R. J. (2018). Origin of spectacular fields of submarine sediment waves around volcanic islands. *Earth and Planetary Science Letters*, 493:12–24.